remote sensing

MDPI

Article

A Two-Step Framework for Mapping, Classification, and Area Estimation of Stand- and Non-Stand-Replacing Forest Disturbances

Isabel Aulló-Maestro [1,2], Saverio Francini [3,*], Gherardo Chirici [4,5], Cristina Gómez [2,6,7], Icíar Alberdi [1], Isabel Cañellas [1], Francesco Parisi [8] and Fernando Montes [1,2]

[1] Institute of Forest Sciences (ICIFOR-INIA, CSIC), 28040 Madrid, Spain; isabel.aullo@inia.csic.es (I.A.-M.); alberdi.iciar@inia.csic.es (I.A.); canellas@inia.csic.es (I.C.); fmontes@inia.csic.es (F.M.)
[2] School of Forest Engineering and Natural Environment (MONTES), Universidad Politécnica de Madrid, 28040 Madrid, Spain; cgomez@uva.es
[3] Department of Science and Technology of Agriculture and Environment (DISTAL), University of Bologna, 40126 Bologna, Italy
[4] Department of Agriculture, Food, Environment and Forestry, Università degli Studi di Firenze, 50145 Firenze, Italy; gherardo.chirici@unifi.it
[5] Fondazione per il Futuro delle Città, 50127 Firenze, Italy
[6] University Institute for Sustainable Forest Management (iuFOR), EiFAB, University of Valladolid, Campus Universitario Duques de Soria, 42004 Soria, Spain
[7] Gestión Forestal Sostenible, iuFOR-UVa, ICIFOR and MNCN CSIC Associated Unit, 34004 Palencia, Spain
[8] Department of Bioscience and Territory, University of Molise, 86090 Pesche, Italy; francesco.parisi@unimol.it
* Correspondence: saverio.francini@unibo.it

Highlights

What are the main findings?

- The calibrated 3I3D algorithm detects forest change areas in Spain (2017–2019).
- The proposed two-step framework classifies forest changes into high- (wildfire, clear-cut) and low-intensity disturbances (thinning, non-stand replacing events).

What is the implication of the main finding?

- Disturbance classification with Random Forest model reached an overall accuracy of 72%, outperforming Support Vector Machine and Neural Network approaches.
- The framework provides a scalable and operational method for annual forest disturbance characterization contributing to forest monitoring and management.

Abstract

In recent decades, forest disturbances have increased in both frequency and intensity, driven by global warming and urbanization. Remote sensing, together with forest disturbance algorithms, offers broad opportunities for forest disturbance monitoring due to its high temporal and spatial resolution. However, operational methods capable of predicting and classifying disturbances while providing official area estimates suitable for national statistics remain scarce. The Three Indices Three Dimensions (3I3D) algorithm has proven effective in identifying forest changes and providing area estimates in Mediterranean ecosystems using Sentinel-2 imagery. Yet, while suitable for change detection, it does not distinguish among disturbance types. Here, we propose a two-step framework for forest disturbance detection and classification, tested in inland Spain for 2018. First, a binary forest change map is produced through an enhanced version of the 3I3D approach. This step incorporates Receiver Operating Characteristic (ROC) analysis to calibrate the algorithm through data-driven threshold selection, allowing adaptation to specific regional

Check for updates

Academic Editor: Eric Casella

Received: 7 February 2026
Revised: 13 March 2026
Accepted: 23 March 2026
Published: 30 March 2026

conditions. Second, detected changes are classified into four disturbance types: wildfire, clear-cut, thinning, and non-stand replacing disturbance, using Sentinel-2 spectral bands, 3I3D-derived metrics, and geometric descriptors of disturbance patches. Three machine-learning classifiers were compared: Support Vector Machine, Random Forest, and Neural Network. The detection step reached an overall accuracy of 82%, estimating that 1.43% of Spanish forests (264,900 ha) were disturbed in 2018. In the classification step, Random Forest achieved the best performance, with an overall accuracy of 72%. Of the detected disturbed area, 69% corresponded to non-stand replacing disturbances, while the remaining area was classified as thinnings (19%), wildfires (26%), and clear-cuts (55%). By integrating freely available Sentinel-2 imagery, remote sensing algorithms, and photo-interpreted reference datasets, this study provides a scalable and operational approach capable of producing annual disturbance maps that combine both detection and classification of high- and low-intensity disturbances, supporting official national-scale estimates of forest disturbance areas.

Keywords: machine learning; Google Earth Engine; Sentinel-2; forest disturbances

1. Introduction

Forests worldwide are shaped by a complex combination of natural and anthropogenic disturbances that influence their dynamics and long-term resilience. At the global scale, climate warming and land use changes have intensified the frequency and intensity of natural forest disturbances worldwide [1,2], such as wildfire, pest outbreak, drought, and windthrow, accelerating decline in marginal forest populations [3] and increasing forest vulnerability to secondary pests and diseases [4,5]. These natural disturbances create canopy gaps that trigger vegetation succession [6]. In Mediterranean regions, such changes are projected to result in more extreme drought conditions and an increase in severe wildfires [7,8]. On the other hand, human-induced disturbances, such as timber harvesting and thinning, have historically shaped forest composition and structure in anthropized ecosystems [9]. While many species have adapted to, or even depend on these disturbance regimes, shifts in intensity, frequency or spatial patterns of disturbance can undermine the role of forests as reservoirs of biodiversity and carbon [2,10,11], and as providers of essential resources and services [12,13]. Integrating ecological forestry practices into forest management can play a vital role in preserving forest biodiversity [14]. Consequently, a detailed and up-to-date understanding of forest disturbance processes at the landscape scale is crucial to inform policy-making and restoration strategies [12,15]. In this context, traditional National Forest Inventories (NFIs) provide accurate and essential field-based information for assessing forest condition and disturbance. Remote-sensing-based algorithms can complement NFIs by supporting spatially continuous and temporally frequent assessments of forest disturbance, improving the characterization of their spatial extent and temporal dynamics [16,17]. The increasing availability of remote sensing data, together with its high spatial and temporal resolution and open accessibility, has made it an essential tool for monitoring forest disturbance [18,19].

Numerous change detection algorithms have been developed and applied worldwide, particularly using Landsat time series data. Among the most widely used are LandTrendr [20], Composite to Change (C2C) [21], and Continuous Change Detection and Classification (CCDC) [22]. Although the Sentinel missions are relatively recent, their higher spatial and temporal resolution offers promising improvements over Landsat for detecting small-scale disturbances. A variety of change detection algorithms have already been developed for the Sentinel-2 platform. For instance, Pacheco-Pascagaza et al. [23] developed and tested a near real-time change detection approach using Sentinel-2 in regions of Mexico and Colombia. Similarly, Jiang et al. [24] introduced DSUNet, an approach that integrates optical Sentinel-2 and SAR Sentinel-1 data to detect forest changes in southwestern China. Other algorithms have been tailored to specific types of disturbance, such as bark beetle infestations [25,26], pine tortoise scale outbreaks [27,28], phenology anomalies [29] and urban expansion [30], among others. It is important to note, however, that most of these algorithms and approaches have been primarily validated in boreal and temperate forests, with relatively few studies focusing on Mediterranean ecosystems [31], which are characterized by higher landscape fragmentation and distinct ecological dynamics [32,33]. Moreover, many of these approaches do not offer a generalizable framework for comprehensive disturbance monitoring.

The Three Indices Three Dimensions (3I3D) algorithm was specifically developed to detect forest disturbance in Mediterranean ecosystems [34]. It has been successfully employed to map forest disturbances in Italy from 2017 to 2020 [35], monitor growing stock volume and carbon stock [36], and differentiate afforestation processes in previously disturbed areas [37,38]. Additionally, when combined with GEDI data, 3I3D has been used to quantify biomass loss associated with these disturbances [39]. To evaluate its performance, 3I3D has been benchmarked against several other disturbance classification algorithms, including LandTrendr [20], Global Forest Change Map [40], and the Two Thresholds Method [41], the latter also developed for the Mediterranean contexts. However, methods based on thresholds may be difficult to apply across different ecosystems, as thresholds can vary depending on forest canopy cover [42].

While numerous algorithms and applications have been employed to map forest disturbance, accurately classifying the type of disturbance remains a more complex challenge. Some efforts have been made in Canada, where Hermosilla et al. [43] and Morin-Bernard et al. [44] classified four and two disturbance types, respectively. In Central Europe, Oeser et al. [45] attempted to distinguish between disturbance agents such as windthrow, beetle outbreaks, and logging. Similarly, in Australia, Nguyen et al. [46] applied an intensity-based classification scheme that differentiated between high- and low-intensity disturbances, including both wildfires and logging. However, significant limitations persist, particularly in the classification of low-intensity disturbances such as selective logging and thinning, which tend to leave subtler spectral signatures [47]. In Europe, comprehensive efforts to classify forest disturbances remain limited. Most existing studies have focused predominantly on high-intensity disturbances (e.g., [45,48]), while relatively few have addressed low-intensity disturbances such as low-intensity thinning (e.g., [49,50]). Expanding disturbance classification frameworks to better capture the full spectrum of forest management and natural disturbance regimes remains a critical research priority.

The goal of this study is to develop a scalable and operational framework capable of monitoring and characterizing both high- and low-intensity forest disturbances. We propose an adaptive, two-step methodological framework that builds upon the 3I3D algorithm. In the first step, we adapt the 3I3D algorithm for binary change detection (change vs. no-change) across regions, incorporating ROC analysis to refine detection thresholds and enhance transferability. This adaptation enhances the sensitivity of the algorithm to subtle spectral changes, which are particularly relevant for forest management applications. In the second step, the detected changes are classified into different types of forest disturbances, enabling the identification of high-intensity (e.g., wildfires, clear-cutting) and low-intensity disturbances (e.g., thinning) by assessing the performance of various classification algorithms, including Support Vector Machine (SVM), Random Forest (RF), and Neural Networks (NN). This hybrid approach enables the classification of forest disturbances with different intensity levels and ensures the applicability across different regions and spatial extents within a specialized and operational framework.

2. Materials and Methods

2.1. Study Area

Forests cover a substantial portion of Spain, accounting for 56% of the national territory, or 28.4 Mha. Of this total, 38% are classified as wooded forests (19.3 Mha), while 18% (9.1 Mha) consist of shrublands. In terms of species composition, broadleaf forests dominate, representing 56% of forested areas, followed by conifers at 37%, and mixed forests at 7%. Approximately 40% of Spanish forests are within protected areas, encompassing 1934 Protected Natural Areas and 16 National Parks [51]. In this study, we focused exclusively on dense forests and plantations with a tree canopy cover of 20% or more, covering an area of 18.5 Mha (Figure 1), based on the Spanish Forest Map 1:25,000 [52]. Open woodlands, primarily used for grazing or agriculture, were excluded due to their sparse canopy cover and the resulting influence of ground reflectance on spectral analyses.

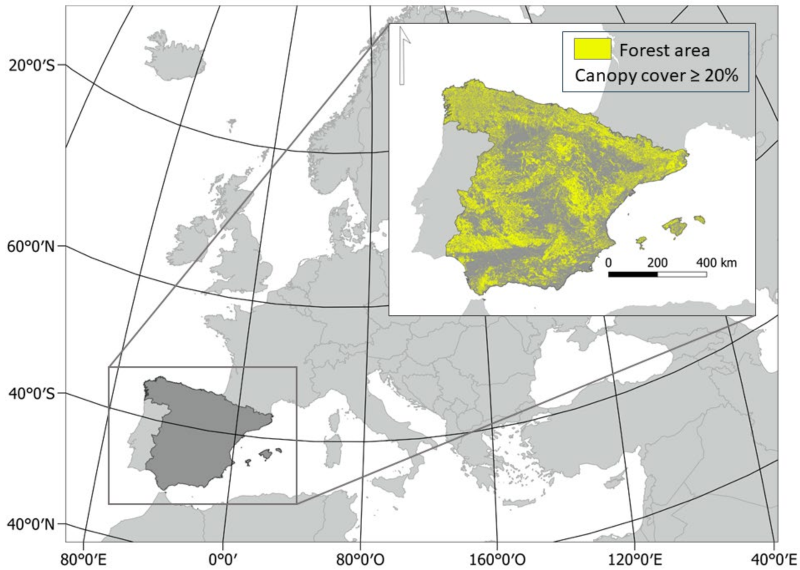

Figure 1. Spanish forest study area comprising dense forests and plantations with canopy cover ≥20%, excluding open woodlands (EPSG: 3035).

Among the various disturbances affecting Spain's forested areas, wildfires stand out as the most significant, impacting significantly larger areas than forest management practices like clear-cutting or thinning. Clear-cutting typically occurs in plantations or intensively managed forests with fast-growing species, where it is often followed by natural regeneration or planting. In contrast, thinning is typically applied to smaller areas within densely reforested or managed stands, aiming to improve forest structure and reduce competition among trees.

2.2. Sentinel-2 Data

The 3I3D algorithm requires the creation of image composites for the change detection year (t = 2018), as well as the preceding (t = 2017) and following (t = 2019) years. The algorithm was implemented using Google Earth Engine (GEE), a cloud-based platform offering an application programming interface (API) for processing large satellite image datasets [53], over Sentinel-2 Level 2A images (2528 images for 2017, 3124 for 2018 and 2771 for 2019). Composites were generated for each year (2017–2019) using imagery acquired between 15 June and 15 August, with cloud cover below 40% [54,55]. Clouds were masked using the Sentinel-2 cloud probability dataset, excluding pixels with a cloud cover probability of 65% or higher [26,56]. Image composites were generated using the median-based medoid compositing approach. Originally developed for Landsat data [57] and later adapted for Sentinel-2 imagery (e.g., [35,58]), this approach assigns to each pixel the surface reflectance values closest to the multidimensional median value among the selected images, providing robustness against outliers and extreme values. For more information on the medoid calculation, see Francini et al. [54]. Image compositing enables the creation of representative data by combining multiple images acquired on different dates, thus minimizing issues such as cloud cover and data gaps.

2.3. Step 1: 3I3D Change Detection

3I3D is an open-access, unsupervised method developed to detect forest change using Sentinel-2 imagery. It evaluates three spectral indices—Normalized Difference Moisture index (NDMI), Normalized Burn Ratio (NBR), and Moisture Stress Index (MSI)—across three consecutive years: the year preceding the target year ($t - 1$), the target year (t), and the year after ($t + 1$). For the 3I3D approach, these indices are computed as follows: NDMI = (B8 − B11)/(B8 + B11), NBR = (B8 − B12)/(B8 + B12) and MSI = B11/B8.

For each pixel in the target median composite image, overall change is characterized using two vectors—*a* and *b*—which connect the points between consecutive years in a three-dimensional spectral index space defined by NBR, NDMI, and MSI, corresponding to two consecutive years [34]. Vector *a* spans from $t - 1$ to t (2017–2018) and vector *b* from t to $t+1$ (2018–2019). Six parameters are derived: the angles ϕ_a and ϕ_b, formed between each vector and the MSI axis; the angles θ_a and θ_b, formed between the projection of each vector onto the NDMI−NBR plane and the NBR axis, and the magnitudes of the two vectors (i.e., $|a|$ and $|b|$). These parameters provide a multi-dimensional characterization of spectral change at the pixel level. A key advantage of 3I3D is that it requires no input parameters or prior calibration, making it a robust and fully automated approach for large-scale forest change detection. Further details on the 3I3D methodology and its implementation in GEE [59] can be found in the original paper by Francini et al. [34].

As a preliminary step before generating the final disturbance map, we applied the 3I3D algorithm to produce a pixel-level map containing the full set of change parameters: angles ϕ and θ, as well as the modules of vectors *a* and *b*. Moreover, we derived the overall change magnitude for each pixel ranging from 0 to 255, calculated as the sum of the two vector modules [34]. Based on this information, a magnitude threshold was then defined to classify pixels as either 'change' or 'no change', as detailed in the following section.

Photointerpretation-Based Reference Data and Threshold Calibration

To determine the magnitude threshold that minimized both commission and omission errors, we conducted a sensitivity analysis on the 3I3D-derived change/no change map. This analysis involved increasing the magnitude threshold in steps of 5 units. For each threshold value, classification performance was assessed using a ROC curve, which plots the relationship between sensitivity (True Positive Rate—TPR) and 1—specificity (False Positive Rate—FPR). The threshold optimizing both sensitivity and specificity was identified.

We conducted a photointerpretation of a stratified random sample of 7555 points. The sampling design used different sampling rates for the no-change (0.00001) and change classes (0.00010), with point locations randomly selected within each class. The photointerpretation followed a consensus-based protocol aligned with the good practices for visual interpretation of remotely sensed data compiled in Jonckheere et al. [60], including the participation of three independent photointerpreters, cross-interpretation of 20% of the sample, a calibration training at the start of photointerpretation and systematic discussion of ambiguous cases.

To match the 20 m spatial resolution of Sentinel-2 imagery, a 10 m buffer was applied around each sampled point. Each buffered point was manually classified as either 0 (no change) or 1 (change) (Figure 2) through visual comparison of orthophotos from the years preceding and following the target year. Very high-resolution (VHR) imagery was used from sources including the Spanish National Plan for Aerial Orthophotography [61] and high-resolution satellite imagery from Google Earth^{TM} [62]. When orthophotos were unavailable for a specific point, Sentinel-2 composites from 2017 and 2019 were compared.

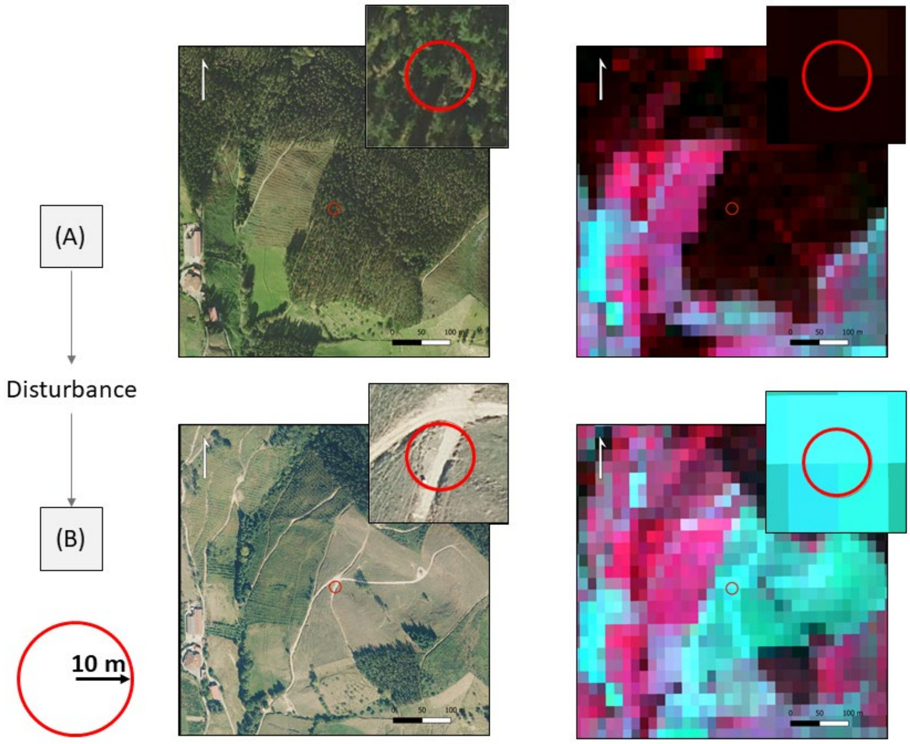

Figure 2. Example of photointerpretation process used for change detection. The left panels show very-high resolution orthophotos (PNOA images) for (**A**) pre-disturbance—2017 and (**B**) post-disturbance—2019. The right panels show corresponding Sentinel-2 medoid composites for the same periods (visualized in False color [B8, B4, B3]). The red circle indicates the sampled plot with a 10 m buffer radius. Insets provide a zoomed view of the buffered area.

2.4. Step 2: Disturbance Classification

Building on the change/no-change map generated by the 3I3D algorithm, our objective was to produce a disturbance map that classified the pixel into one of the predominant disturbance types commonly observed in Spain (Figure 3). We focused on major, well-represented disturbances in the study area, excluding subtle changes like variations in vegetation moisture or rare events like windthrow, which were insufficiently represented. The disturbance types included in this study are two high-intensity disturbances: wildfires and clear-cutting, and two low-intensity disturbances: thinning and non-stand replacing. The non-stand replacing class, as defined by Coops et al. [63], includes areas flagged by 3I3D as changed but not attributable to the three specific disturbance types during photointerpretation.

To achieve this, we evaluated the performance of three classification algorithms: Support Vector Machine (SVM), Random Forest (RF) and Neural Network (NN).

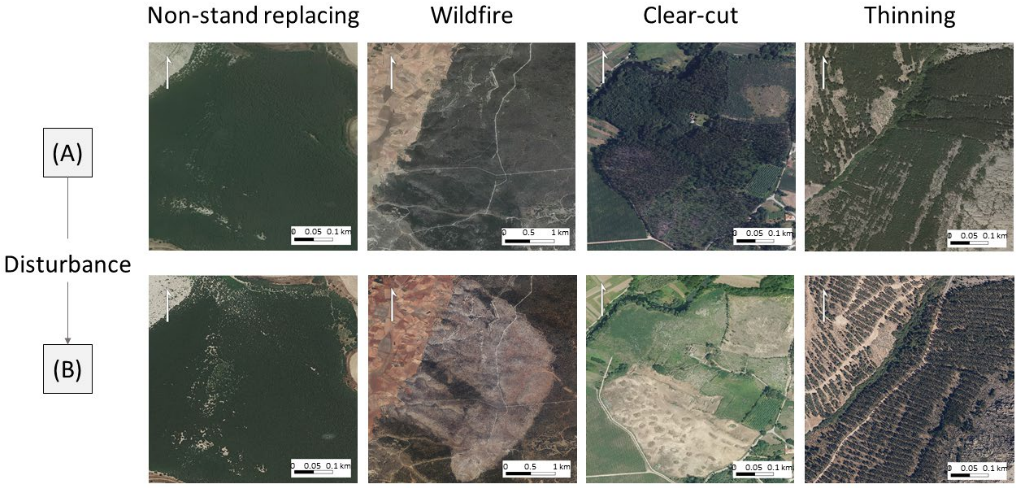

Figure 3. Examples of forest disturbances for (**A**) pre-disturbance—2017 and (**B**) post-disturbance—2019. Columns illustrate the disturbance types considered in the study: non-stand replacing, wildfire, clear-cut, thinning.

2.4.1. Training Dataset and Variable Selection

For training, a dataset of 1524 polygons identified as 'change' in the first step was randomly sampled and photointerpreted. Each polygon was assigned to one of four categories: (0) non-stand replacing disturbance, (1) wildfire, (2) clear-cut or (3) thinning (Table 1).

Table 1. Training data for classification of disturbance type. Number of polygons photointerpreted for each class.

Change Class	Number of Polygons	Average Polygon Size (ha)
Non-stand replacing	792	22
Wildfire	70	219
Clear-cut	483	8
Thinning	179	16

We initially considered a comprehensive set of 47 variables, including spectral metrics, 3I3D change metrics [34], and geometrical metrics [43]. To ensure the robustness of our final variable selection, we employed an iterative process in which uncorrelated variables were progressively selected while evaluating the classification results at each iteration. When two variables exhibited multicollinearity (Pearson correlation coefficient, $R > 0.70$) expert criteria were used to select the one considered more relevant for the study regarding ecological and spectral characteristics. The resulting single, consistent set of variables was used throughout both the training and validation phases of the classification process.

2.4.2. Support Vector Machine Classification

SVM, first described by Boser et al. [64] and widely applied to forest land cover classification [65], are binary classification algorithms that aim to find the optimal hyperplane that maximizes the margin between classes—defined by the closest training samples, known as support vectors. To handle non-linearly separable data, SVM utilizes Kernel functions to project the data into a higher dimensional feature space where linear separation becomes possible. For multiclass classification, we employed the fitcecoc function in Matlab® R2024b, which implements the Error-Correcting Output Codes (ECOC) framework to decompose the problem into multiple binary classification tasks. For each binary learner, the function optimizes parameters such as the box constraint, Kernel function (e.g., Gaussian, linear, or polynomial) and Kernel scale. Given the class imbalance in our training dataset (Table 1), we applied class weighting inversely proportional to class frequencies. This strategy mitigates the bias towards majority classes, helping to ensure balanced learning and improve generalization across all classes.

2.4.3. Random Forest Classification

RF, depicted by Breiman et al. [66] is an ensemble learning method that constructs multiple classification decision trees by resampling the training data for each classification tree. Within each tree, the training observations are iteratively assigned labels through a number of splits, ranging from 1 to $n - 1$, where n represents the total number of observations in the training dataset. Specifically, at each node, the algorithm selects the predictor that yields the greatest gain in the Gini diversity index across all possible splits. To implement and optimize the ensemble of decision trees, we employed the fitcensemble function in Matlab®, which applies the bagging technique. In this approach, each tree is trained on a bootstrap sample of the data, and at each node, a random subset of predictors is considered for splitting. The fitcensemble function allows fine-tuning of key hyperparameters, such as the number of learning cycles (trees), learning rate, and minimum leaf size (the minimum number of observations per terminal node). As with SVM, we addressed class imbalance incorporating class weights during model training, assigning weights inversely proportional to class frequencies to ensure fair representation of all classes.

2.4.4. Neural Network Classification

Neural Networks have been widely used for analyzing remote sensing data [67]. In this study we trained an NN classifier using Bayesian optimization via the fitcnet function in Matlab®. This approach permitted the automatic tuning of several hyperparameters, including the number and size of hidden layers, activation functions (e.g., Rectified Linear Unit [ReLU], hyperbolic tangent, sigmoid, or none), weight initialization methods (such as Glorot or He initializer) and the regularization strength (Lambda). The network architecture employed for classification consisted of up to three fully connected layers. In each layer, the output from the preceding layer is transformed by a weight matrix and passed through an activation function. The final layer applies a softmax activation to produce class probabilities and predicted labels. The Glorot initializer samples weights from a uniform distribution with a mean of 0 and variance of $2/(n_{input} + n_{output})$, while the He initializer employs a variance of $2/n_{input}$, making it more suitable for ReLU activations. The training process employed default settings: a maximum number of 1000 iterations, a loss tolerance (1×10^{-6}), step tolerance (1×10^{-6}), and a validation patience of 6 iterations. To address class imbalance in the training data, we incorporated class weights inversely proportional to class frequencies, ensuring equitable representation across all classes during learning [68].

2.4.5. Classification Accuracy Assessment

To evaluate the performance and robustness of each classification model, we performed 10-fold cross-validation for each learner, withholding 10% of the 1524 training samples in each fold for validation [69,70]. Model performance was assessed using confusion matrices, from which we derived omission and commission errors, overall accuracies and class specific metrics including the Area Under the Curve for the Receiver Operating Characteristic (AUC_{ROC}), and Area Under the Precision-Recall Curve (AUC_{PR}).

The AUC_{ROC} was computed by progressively adjusting the decision threshold based on class scores, as described by Valavi et al. [71]. The AUC_{PR} was obtained using the procedure outlined by Hughes-Oliver [72]. One per class AUC_{ROC} and AUC_{PR} (one vs. all) was applied in the case of disturbance classifications.

To address the effects of class imbalance, we computed the Matthews Correlation Coefficient (*MCC*), which quantifies the correlation between the observed and predicted binary classifications [73], and the *F*1-*score* per class, which is the harmonic mean of precision and recall:

$$MCC = \frac{TP \cdot TN - FP \cdot FN}{\sqrt{(TP + FP) \cdot (TP + FN) \cdot (TN + FP) \cdot (TN + FN)}}$$

$$F1score_i = \frac{2(TP_i/(TP_i + FP_i))(TP_i/(TP_i + FN_i))}{TP_i/(TP_i + FP_i) + TP_i/(TP_i + FN_i)}$$

where *TP*, *TN*, *FP* and *FN* refer to the sum of True Positives, True Negatives, False Positives and False Negatives, respectively, across the disturbance classes, in the confusion matrix. The *MCC* ranges from −1 to +1, where +1 represents a perfect prediction, 0 indicates a random prediction, and −1 indicates a complete disagreement between the prediction and the true label.

Following the methodology proposed by Olofsson et al. [74], overall and per-class accuracies were computed by weighting the confusion matrices' accuracies by the proportion of area mapped as each class. The proportion of area estimations, standard error and confidence intervals (Table A3) are calculated as:

$$\hat{p}_{.k} = \sum_{i=1}^{q} W_i \frac{n_{ik}}{n_i}$$

$$S^2(\hat{p}_{.k}) = \sum_{i=1}^{q} \left(W_i \hat{p}_{ik} - \hat{p}_{ik}^2 \right) / (n_i - 1)$$

$$CI_i = \pm 1.96 \times S(\hat{p}_{.k})$$

where *W* represents the proportion of area mapped as class *i*, n_{ik} is the entry of the confusion matrix in the *i* row and *k* column, and *ni* is the number of sampling points in class *i*. $S^2(\hat{p}_{.k})$ is the proportion of area estimated for class *k*, where $\hat{p}_{ik}$ is calculated as n_{ik}/n_i. CI_i is the confidence interval of class *i* area estimate.

3. Results

3.1. 3I3D Change Detection

The results of the ROC analysis for change detection, based on varying magnitude thresholds, are presented in Table A1. A threshold value of 205 was identified as optimal for generating the change map, yielding an overall accuracy of 82%, a False Positive Rate (FPR) of 0.17 and a True Positive Rate (TPR) of 0.73.

The confusion matrix (Table 2) shows a balanced distribution of producer accuracies across classes. Low omission error rates can be observed, increasing Producer's accuracy at the expense of User's accuracy. This pattern suggests a tendency toward over-detection in ambiguous cases and, consequently, inflating commission errors.

These intermediate results were further processed to generate the final 3I3D change map using a threshold value of 205. The total area identified as change was 264,900 ha, accounting for 1.43% of the study area.

Table 2. Confusion matrix based on 7555 sample points generated using the 3I3D algorithm with a magnitude threshold of 205.

Predicted \ Reference	Change	No Change	User's Accuracy	Commission Error
Change	804	1081	43%	57%
No change	301	5369	95%	5%
Producer's accuracy	73%	83%	Overall Accuracy 82%	
Omission error	27%	17%		

3.2. Classification Models

The initial pool of 47 variables was reduced to a final set of 16 (Table A2). Correlation analysis showed that wildfires were well characterized by higher perimeter standard deviation and higher shape index (Figure 4a,b). Clear-cuts were associated with lower fractal dimension and higher SWIR1 standard deviation (Figure 4c,d). Thinnings were characterized by a lower module *b* (Figure 4e), whereas other disturbances class were associated with a lower module *a* (Figure 4f).

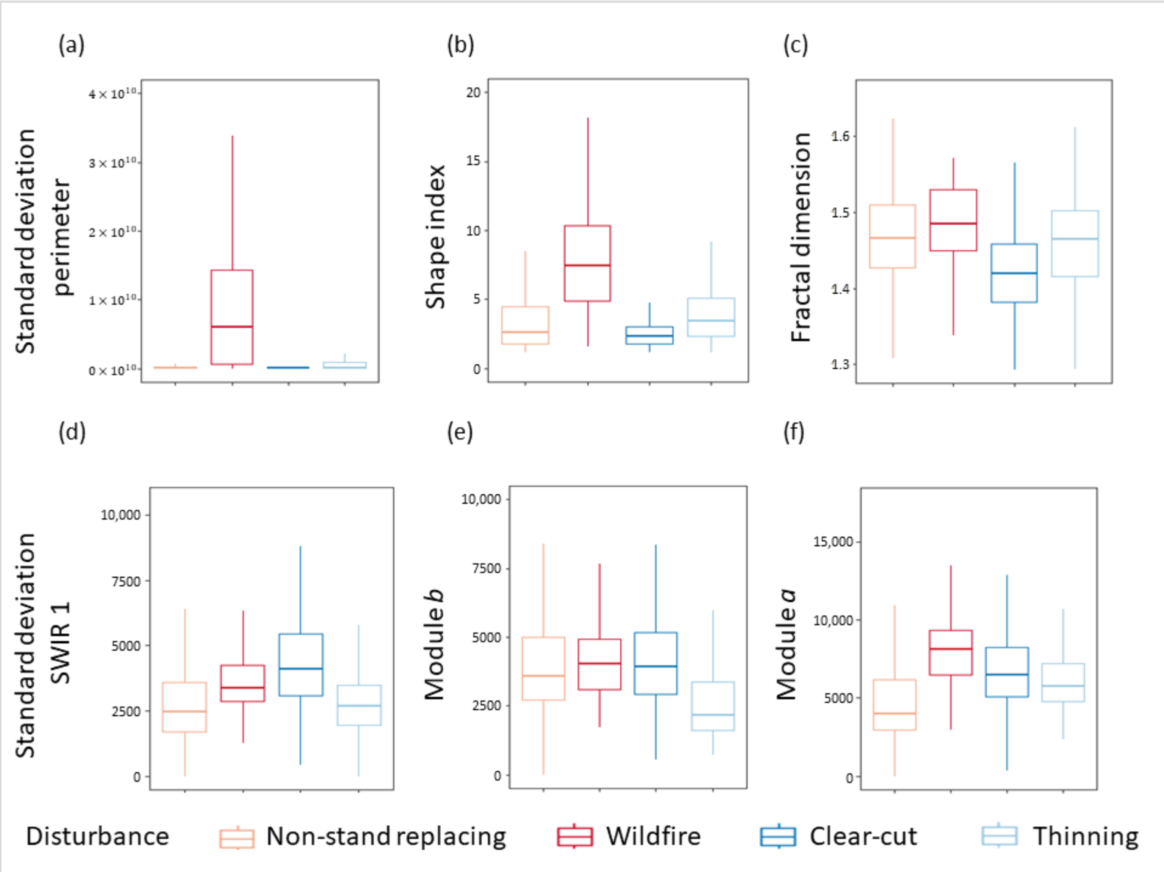

Figure 4. Six out of the sixteen variables used are shown, selected for their capacity to discriminate changes among disturbance types: non-stand replacing, wildfires, clear-cut, and thinning. (**a**) Standard deviation of perimeter, (**b**) Shape index, (**c**) Fractal dimension, (**d**) Standard deviation of SWIR 1, (**e**) Module *b*, and (**f**) Module *a*.

Among the classifiers, RF achieved the highest performance, with an overall accuracy of 72.0% and an *MCC* of 0.56. Hyperparameters were optimized resulting in a configuration of 492 trees and a minimum leaf size of 3 samples. SVM ranked second, with an overall accuracy of 71.0% and *MCC* of 0.52. The SVM was implemented using a Gaussian kernel with a box constraint value of 0.0034 and kernel scale of 5.24. NN followed with an overall accuracy of 67.8% and *MCC* of 0.47; for NN the He initializer was used for the layer weights, the hidden layer size was set to 13, and the lambda value was 0.0047. The corresponding accuracies and confusion matrices for each classifier are presented in Tables 3 and 4.

Table 3. Overall accuracy, Area Under the Precision-Recall Curve (AUC_{PR}) and Area Under the Curve for the Receiver Operating (AUC_{ROC}). Value for Random Forest, Support Vector Machine and Neural Network classification methods for non-stand replacing disturbances, wildfires, clear-cut and thinning.

	Random Forest		**Support Vector Machine**		**Neural Network**	
Overall accuracy	72.0%		71.0%		67.8%	
	AUC_{PR}	AUC_{ROC}	AUC_{PR}	AUC_{ROC}	AUC_{PR}	AUC_{ROC}
Non-stand replacing	0.88	0.86	0.86	0.81	0.87	0.84
Wildfire	0.67	0.94	0.58	0.90	0.68	0.94
Clear-cut	0.66	0.84	0.66	0.79	0.64	0.83
Thinning	0.55	0.83	0.53	0.79	0.53	0.84

Table 4. Confusion matrix value for Random Forest, Support Vector Machine and Neural Network classification methods for non-stand replacing disturbances (NSR), wildfires, clear-cut and thinning: User's accuracy (User's acc), commission error (CE) and F1-score.

	NSR	**Wildfire**	**Clear-Cut**	**Thinning**	**User's Acc**	**CE**	**F1**
			Random Forest				
Non-stand replacing	594	9	72	33	83.9%	16.1%	0.79
Wildfire	16	49	18	2	57.6%	42.4%	0.63
Clear-cut	149	7	356	46	63.8%	36.2%	0.68
Thinning	33	5	37	98	56.6%	43.4%	0.56
Producer's accuracy	75.0%	70.0%	73.7%	54.7%			
Omission error	25.0%	30.0%	26.3%	45.5%			
			Support Vector Machine				
Non-stand replacing	551	6	96	34	80.2%	19.8%	0.75
Wildfire	26	50	31	9	43.1%	56.9%	0.54
Clear-cut	142	5	294	34	61.9%	38.1%	0.61
Thinning	73	9	62	102	41.5%	58.5%	0.48
Producer's accuracy	69.6%	71.4%	60.9%	57.0%			
Omission error	30.4%	28.6%	39.1%	43.0%			
			Neural Network				
Non-stand replacing	523	3	62	14	86.9%	13.1%	0.75
Wildfire	49	58	28	11	39.7%	60.3%	0.54
Clear-cut	147	3	336	37	64.2%	35.8%	0.67
Thinning	73	6	57	117	46.2%	53.8%	0.54
Producer's accuracy	66.0%	82.9%	69.6%	65.4%			
Omission error	34.0%	17.1%	30.4%	34.6%			

The non-stand replacing disturbance class achieved the highest User's accuracy across all three classification techniques, particularly with RF. In contrast, wildfires showed the highest Producer's accuracy when classified with SVM and NN. Thinning was the most challenging class to identify, exhibiting the highest commission and omission errors across models—except in the case of NN, where wildfires had higher commission errors (Table 4).

3.3. Forest Disturbance Classification Map

Based on the disturbance classification results, we generated a comprehensive classification map (Figure 5—Step 2) and classification probability map (Figure A1) of the four-disturbance classes, modeled using the Random Forest algorithm: non-stand replacing disturbance, wildfire, clear-cut, and thinning. Non-stand replacing disturbances accounted for 69% of the total disturbed area. When excluding non-structural changes, the remaining disturbed area was composed of 19% thinning, 26% wildfires, and 55% as clear-cut events.

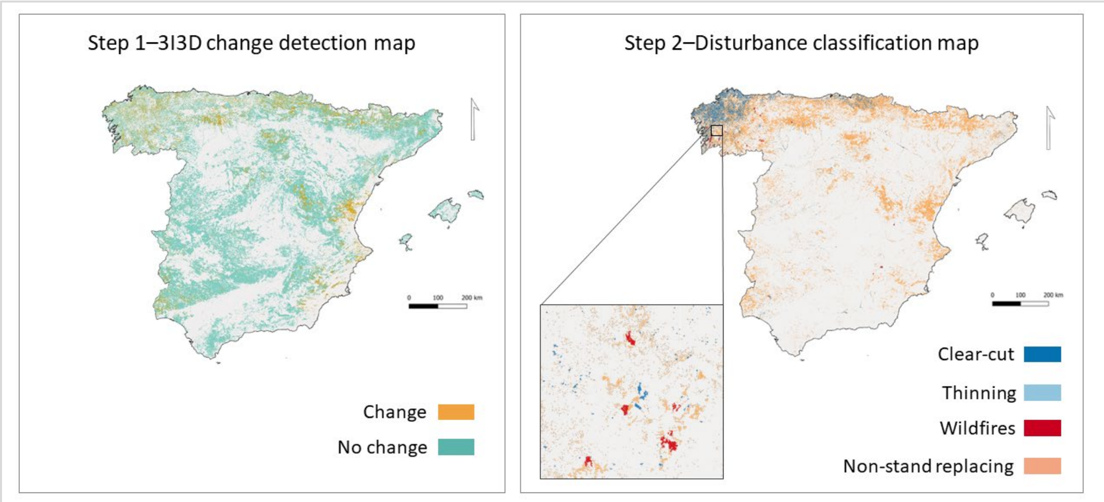

Figure 5. Results of the two-step framework for national-scale forest disturbance monitoring in mainland Spain and the Balearic Islands for the year 2018. Step 1: 3I3D change detection map. Step 2: disturbance classification map derived from Random Forest algorithm including non-stand re-placing disturbances, wildfires, clear-cuts, and thinning. The inset provides a zoom-in illustrating the different disturbance classes (EPSG: 32629).

The non-stand-replacing disturbance class was the most frequent, comprising 1.36 million polygons. However, it had the smallest average polygon size (0.14 ha), resulting in a total area of 184,000 ha. In contrast, wildfires had the largest average polygon size (105.86 ha), with a total affected area of 21,400 ha. Thinning disturbances averaged 1.52 ha per polygon and covered 15,300 ha in total, while clear-cuts had an average size of 1.44 ha, accounting for 44,200 ha overall (Table A3). Per class accuracies following Olofsson et al. [74] are shown in Table A3, summing a weighted overall accuracy of 0.77.

4. Discussion

Mediterranean forests have long experienced ecosystem fragmentation, primarily driven by historical human activities [75]. These forests exhibit distinctive disturbance patterns and a faster recovery rate compared to boreal or temperate forests, resulting in a distinctive post-disturbance spectral response [32]. Unfortunately, Mediterranean forests are particularly vulnerable to degradation processes due to land abandonment and the ongoing impacts of climate change, which exacerbate both the frequency and intensity of forest disturbances [76]. Comprehensive research into these disturbance dynamics is therefore imperative, given their far-reaching implications for biodiversity, as well as for the economic, social, and ecological sustainability of forest ecosystems [1,2].

To address these needs, we implemented an adaptive two-step framework aimed at producing a national-scale forest disturbance map for Spain. In the first step, we applied the 3I3D algorithm across the national territory to generate a binary change/no-change map based on spectral variables. An optimal threshold for change detection was identified using ROC analysis, allowing us to differentiate between change and no-change pixels. Detected changes included both high-intensity (e.g., wildfire, clear-cutting) and low-intensity disturbance (e.g., thinning) as well as subtle, non-stand replacing disturbances. In the second step, we employed a Random Forest classifier to categorize the change pixels into four distinct disturbance classes—wildfire, clear-cut, thinning, and non-stand replacing—using a combination of spectral metrics, 3I3D change metrics, and geometrical features as input variables.

4.1. Performance of Two-Step Framework

The use of summer composites in the 3I3D algorithm to detect inter-annual changes benefits from reduced cloud cover in the Mediterranean region and from peak vegetation photosynthetic activity during this period, which enhances spectral contrast between disturbed and undisturbed areas. However, it also introduces variability related to the timing of disturbance events. Disturbances occurring between acquisition dates may be partially smoothed within a composite, while events spanning consecutive years may be detected more than once. To account for this variability, the proposed two-step approach incorporates detailed information from consecutive temporal intervals ($(t-1)-t$ and $t-(t+1)$) together with Sentinel-2 spectral reflectance features during the classification step. This integration helps to stabilize disturbance attribution across years and reduces ambiguity associated with the seasonal compositing strategy.

The proposed two-step framework demonstrated a robust capacity to detect forest disturbances across heterogeneous Mediterranean landscapes. The change/no-change map achieved an overall accuracy of 82%, consistent with previous applications of the 3I3D algorithm in Mediterranean environments [34]. This accuracy is primarily supported by the calibration of the change detection threshold through ROC curve analysis obtaining relatively low omission error for change areas.

The high sensitivity in the change detection step increases the detection rate at the expense of relatively low User's accuracy, which is mitigated in the subsequent classification step by reallocating many falsely detected change pixels to the non-structural disturbance class, thereby reducing overall classification error.

Producer's accuracy varied across disturbance classes, with the highest values observed for clear-cut (74%), followed by wildfire (70%), and thinning (55%). These results align with trends reported in previous studies. For instance, Pitkänen et al. [77], working in British Columbia, Canada, observed substantially lower Producer's accuracy for thinning (20.4%) compared to clear-cut areas (80.2%) when applying sensitivity-based thresholds.

The threshold calibration step enhances the robustness of the 3I3D method, improving its adaptability to varying forest conditions and supporting its applicability across different forest types. This step also reduces misclassifications in change areas during the subsequent disturbance classification stage. In addition, threshold calibration provides flexibility to adjust the balance between sensitivity and specificity according to the objectives of the analysis and the characteristics of the disturbance regime. Li et al. [78] further demonstrated that forest-type specific threshold methods can substantially improve disturbance detection across contrasting forest types, reinforcing the importance of threshold calibration in large-scale monitoring frameworks.

4.2. Influence of Spatial Resolution and Disturbance Size in Forest Disturbance Classification

Many change detection algorithms rely on Landsat time series data, which offers lower spatial resolution (30 m) compared to Sentinel-2 (20 m). For example, Miguel et al. [31] employed the CCDC-SMA method to monitor disturbance trends, including non-stand replacing events, across climatic gradients in Spain, achieving a Producer's accuracy of 85.6% for disturbed patches larger than 0.5 ha (2016–2020). Similarly, Nguyen et al. [46]

applied a Random Forest model with LandTrendr predictors to a 30-year Landsat time series in Australia, obtaining Producer's accuracies of 69.4% for selective logging and 78.9% for primary and secondary disturbances.

Accuracies can also vary depending on the size of the disturbances. Jarron et al. [79], using the C2C algorithm in British Columbia, Canada, assessed detection performance across disturbance object of varying sizes: >5 ha, 2 ha, and <2 ha. They found that Producer's accuracy increased significantly for larger disturbances, reaching 93.0% for objects over 5 ha, compared to just 66.0% for both medium and small disturbances. This underscores the inherent challenge of detecting small-scale disturbances using remote sensing.

Imbalance in the frequency and spatial extent of classes may lead to misclassification or underestimation of rare disturbance classes. In our study, wildfires or thinnings are less representative in terms of frequency. As noted by Altalhan et al. [80] algorithm-level approaches such as class weighting can help address this issue. In addition, the evaluation metrics used in this study such as AUC_{PR} have proven useful for assessing performance under imbalance data conditions [80,81]. Although this remains a limitation and results should be interpreted as a simplified representation of reality, future studies could further address class imbalance by integrating both data-level technics and algorithm level techniques.

While lower spatial resolution imagery can limit the detection of small-scale disturbances, higher-resolution data—such as that provided by Sentinel-2—offers improved sensitivity to finer spatial changes. Nevertheless, excluding disturbances below a certain size threshold may enhance overall classification accuracy by minimizing noise introduced by minor or ambiguous changes. This approach, while beneficial for reducing false positives, may also lead to the omission of low-intensity disturbances that affect smaller areas.

While smaller events may remain undetected, the algorithm effectively captures the overall area affected by wildfire, supporting its utility for large-scale disturbance assessments.

4.3. Influence of Classification Algorithms and Input Features

In the final classification map, the effectiveness of RF for disturbance classification is well established [82–85], particularly when incorporating spectral, temporal, and topographic metrics [43,45]. Although deep learning and other novel approaches are currently gaining popularity for studying disturbances [86–88], numerous studies have demonstrated that the algorithms evaluated in this study, RF, SVM and NN, perform reliably for disturbance classification [89,90]. Moreover, using more complex methods is not always necessary when established algorithms sufficiently meet the research objectives [91].

Among spectral variables, the Shortwave Infrared (SWIR) and Near-Infrared (NIR) bands, have been identified as key predictors for detecting forest disturbances [92]. Our analysis utilized a combination of the Blue, NIR and two SWIR bands, along with geometric and 3I3D change-detection metrics, as input features for the classification.

4.4. Low-Intensity Disturbance Characterization

Mediterranean regions exhibit greater variability in forest cover compared to temperate and boreal forests [32]. This heterogeneity may impact the classification accuracy, particularly for low-intensity disturbance classes such as thinning. Accurately detecting low-intensity disturbances remains a significant challenge in satellite-based forest change monitoring [44]. Furthermore, the fragmented nature of Mediterranean landscapes tends to produce smaller, more localized disturbances, further complicating the detection of subtle changes [32]. Many existing change detection algorithms are poorly suited for capturing low-intensity disturbances [47], as they often prioritize abrupt, high-magnitude changes over more gradual or diffuse alterations [93].

https://doi.org/10.3390/rs18071038

In our study, the use of ROC curve analysis to define an optimal change threshold enable the inclusion of subtle, non-stand replacing disturbances. These disturbances included variations in reflectance that do not noticeably reduce forest cover, including those caused by pests, drought, or differences in the phenological traits of the composites, some of which may serve as important indicators of forest health and resilience. Further analysis of changes classified as non-structural may require field data support. In addition, our approach also captured high-intensity events such as wildfires or clear-cuts, and low-intensity structural changes such as thinning.

Omission errors in the first step (pixels classified as no change where any disturbance has occurred) are propagated through the two-step approach, reducing the User's accuracy of the global classification for wildfire, clear-cut and thinning classes. Depending on the final purpose of the analysis, the magnitude threshold may be determined as the ROC optimal or that which maximizes either the sensitivity or the specificity in the first step.

4.5. Comparison with Large-Scale EO Monitoring System

Recently released DIST-ALERT [94] tracks vegetation disturbances using 30m Harmonized Landsat Sentinel-2 dataset obtaining Producer's accuracies ranging from 60 to 75% depending on the type of disturbance and biome considered. The Global Land Analysis & Discovery (GLAD) in collaboration with Global Forest Watch (GFW) [40] provides information for forest cover loss in a Google Earth Engine Application [95] from 2000 to 2024 based on Landsat time series analysis. However, the product functions primarily as an indicator of change rather than as a tool for precise area estimation.

For wildfire monitoring, several platforms are available, such as the Burnt Area maps from the Copernicus Land Monitoring Service [96]. This platform gives daily updated information for burnt areas worldwide from 2023 to 2025, and monthly updates from July 2018 onward, with a 300m spatial resolution. Similarly, Global Wildfire Information System (GWIS) annual statistics for Spain [97], based on MODIS data, report a total of 47,076 ha burned across 207 fires. Regarding National statistics, official records from MITECO [98] indicate that approximately 2000 wildfires $\geq$1 ha occurred in Spain in 2018, substantially more than the 202 wildfires identified in our study. However, the total burned area in our results (21,400 ha) closely matches the 25,000 ha reported in the national statistics.

Overall, our results are closer to GWIS in terms of the number of detected fires, whereas the total burned area is more consistent with official national statistics. The lower number of wildfires identified in our study likely reflects the loss of small fires. Differences in the minimum mapping unit (MMU) further affect these comparisons. Both GWIS and our analysis rely on pixel-based detections (300 m and 20 m resolution, respectively), which may overlook small events or aggregate multiple disturbances into a single fire polygon. Additionally, GWIS estimates do not apply a forest mask and therefore include fires across all land-cover types, whereas national statistics include fires occurring in open woodlands that were masked out in our study.

4.6. Operational Implications, Limitations and Future Directions

In this study, open woodlands were excluded from the change detection analysis, as spectral index variations in these areas primarily reflect changes in ground vegetation rather than alterations in canopy structure. This limitation is inherent to the spatial resolution of Sentinel-2 imagery, which also restricts the detection of damage at individual-tree level, such as tree mortality caused by bark beetle attacks. Nevertheless, finer-resolution data can enable the detection of canopy-level changes through image segmentation techniques that identify individual tree crowns. For instance, Karlson et al. [99] used Worldview imagery combined with GEOBIA (Geographic Object-Based Image Analysis) to delineate individual tree crowns and clusters in open woodlands across West Africa. More recently, Ji et al. [100] applied the BlendMask deep learning algorithm to Worldview-3 imagery, successfully segmenting tree crowns across sites with varying tree densities. LiDAR data has also proven effective for this purpose, as demonstrated by Sun et al. [101], who used the YOLO-v4 deep learning model for individual tree crown detection.

From an operational perspective, this framework has strong potential to complement National Forest Inventories by providing spatially explicit and temporally consistent information on forest disturbance dynamics. Future work should focus on extending the framework to multi-year disturbance trajectories and thoroughly evaluating its transferability to other Mediterranean regions. Such developments would further enhance the capacity of forest monitoring and management systems, which will support adaptive policy implementation, and climate change mitigation strategies.

5. Conclusions

Five main conclusions can be drawn from this study.

First, the proposed two-step framework offers a scalable and tailored approach for forest disturbance mapping by integrating the 3I3D algorithm for change detection with Random Forest classification. This combination allows not only accurate detection but also a meaningful reassignment of apparent false positives, as changes that do not substantially alter stand density are reclassified as non-stand replacing disturbances.

Second, the use of photo-interpreted training samples, combined with geometric attributes and 3I3D-derived metrics, enhances classification accuracy. The approach demonstrates that leveraging complementary data sources strengthens the ability to discriminate among disturbance types.

Third, among the tested classifiers, Random Forest achieved the best results, surpassing both Support Vector Machine and Neural Networks. Its ability to reliably categorize both high- and low-intensity disturbances, particularly thinning, underscores its robustness in operational applications and confirms that it should be the first choice in similar studies.

Fourth, our method shows strong potential for generating annual disturbance maps and supporting near-real-time monitoring, while also enabling long-term assessments of disturbance extent, intensity, and frequency. In addition, the implementation of ROC analysis in the first step enhances the scalability and adaptability of the framework to different regions and objectives. By providing both detection and categorization in a coherent framework, it delivers information directly usable in management and policy contexts, forming a solid basis for evidence-based strategies that promote biodiversity conservation and economic sustainability.

Crucially, our method confirms the importance of systematically integrating remote sensing data into official forest monitoring programs, enabling more spatially detailed information and more accurate aggregated estimates, thereby strengthening the Spanish National Forest Inventory.

Author Contributions: Conceptualization, I.A.-M., F.M. and S.F.; Methodology, I.A.-M., F.M., C.G. and S.F.; Validation, I.A.-M. and F.M.; Resources, F.M., I.A.; Data Curation, I.A.-M. and F.M.; Writing—Original Draft Preparation, I.A.-M.; Writing—Review & Editing, I.A.-M., F.M., S.F., G.C., F.P., C.G., I.A. and I.C.; Supervision, F.M., C.G. and S.F.; Funding Acquisition, F.M., I.C. All authors have read and agreed to the published version of the manuscript.

Funding: This study was partially supported by the following projects: PID2020-119204RB-C21 Conservation vs. management: Monitoring and evaluation of ecosystem services across forest management gradients funded by the Spanish Ministry of Science, Innovation and Universities. 2481s/2017 Vulnerability and resilience of old-growth forest against changes in management and climate: implications for forest management in National Parks funded by OAPN. WHAT-IF project, which is supported by Fundación Biodiversidad of MITECO in the frame of PRTR, funded by European Union—NextGenerationEU. FORWARDS, H2020 project funded by the European Commission, number 101084481 call HORIZON-CL6-2022-CLIMATE-01-05. MONIFUN, H2020 project funded by the European Commission, number 101134991 call HORIZON-CL6-2023-CircBio-01-14. NextGenCarbon, H2020 project funded by the European Commission, number 101184989 call HORIZON-CL5-2024-D1-01-07. PNRR, funded by the Italian Ministry of University and Research, Missione 4 Componente 2, "Dalla ricerca all'impresa", Investimento 1.4, Project CN00000033.

Data Availability Statement: The data that support the findings of this study are openly available in Digital CSIC at https://doi.org/10.20350/digitalCSIC/17553.

Conflicts of Interest: The authors declare no conflicts of interest.

Appendix A

Table A1. Curve ROC results. Magnitude cutoff value. FPR = False Positive Rate. TPR = True Positive Rate. Gray presents the optimum magnitude cutoff.

Magnitude	FPR	TPR
180	0.52	0.87
185	0.44	0.83
190	0.40	0.82
195	0.34	0.80
200	0.24	0.76
205	0.17	0.73
210	0.13	0.67
215	0.11	0.62
220	0.10	0.57
225	0.07	0.48
230	0.06	0.40
235	0.04	0.33
240	0.03	0.28
245	0.03	0.24

Table A2. Final variables used for the classification of the polygons identified as change by the 3I3D algorithm.

Statistic	Variables
	Spectral metrics
Standard deviation	B
Average, Standard deviation	NIR
Standard deviation	SWIR1
Average	SWIR2
	3I3D metrics
Average	Magnitude
Average	Module *a*
Average, Standard deviation	Module *b*
Standard deviation	p_θ_a
Average	p_ϕ_a
Standard deviation	p_ϕ_b
	Geometrical metrics
Standard deviation	Perimeter
Average	Compactness
Average	Fractal dimension
Average	Shape index

Table A3. Random Forest classification map results including class-level statistics and map accuracy estimations. *W* represents the proportion of area mapped as class *i*, $\hat{U}_i$ the estimated User's accuracy for class *i*, $\hat{P}_i$ the estimated user's accuracy for class *i*, CI (%) the 95% confidence interval of the estimated proportion of area of class *i*, and Weighted OA is the estimated overall accuracy.

Change Class	Number Polygons	Area per Class (ha)	Polygon Size (ha)				W	$\hat{U}_i$	$\hat{P}_i$	CI (%)
			Average	Standard Deviation	Minimum	Maximum				
Non-stand replacing	1,360,000	184,000	0.14	24,190	0.04	1491	0.69	0.89	0.84	2.12
Wildfire	202	21,400	105.86	1.9×10^6	0.12	1431	0.08	0.79	0.58	1.05
Clear-cut	30,641	44,200	1.44	27,321	0.6×10^{-5}	78	0.17	0.52	0.64	1.86
Thinning	10,083	15,300	1.52	50,924	0.17×10^{-4}	205	0.06	0.41	0.57	1.25
	Total area =	264,900					Weighted OA = 0.77			

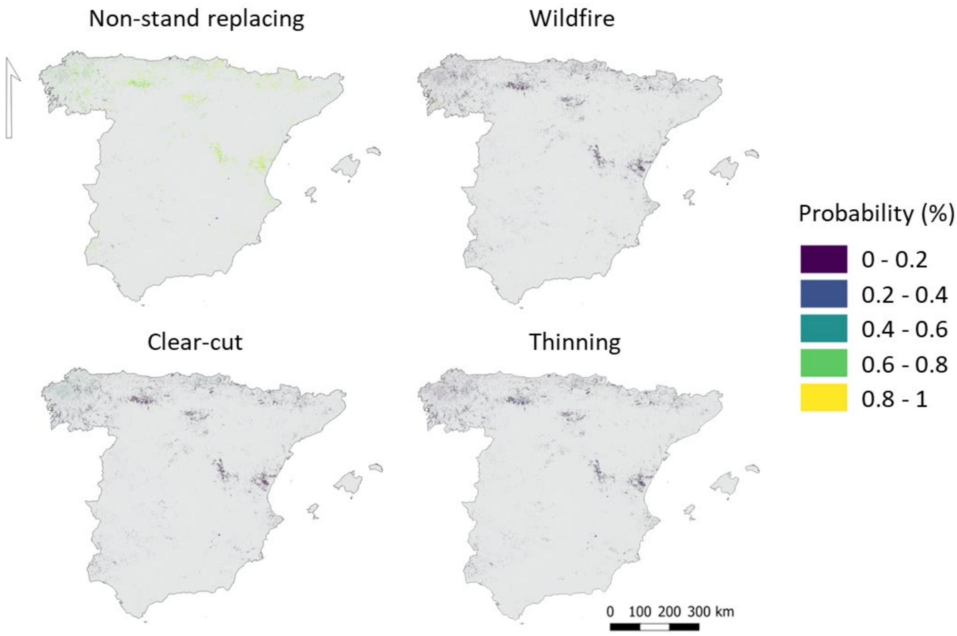

Figure A1. Random Forest classification probability maps for non-stand replacing disturbances, wildfires, clear-cuts and thinnings (EPSG: 32629).

References

1. Patacca, M.; Lindner, M.; Esteban, M.; Cordonnier, T.; Fidej, G.; Gardiner, B.; Hauf, Y.; Jasinevičius, G.; Labonne, S.; Linkevičius, E.; et al. Significant increase in natural disturbance impacts on European forests since 1950. *Glob. Change Biol.* **2023**, *29*, 1359–1376. [CrossRef] [PubMed]
2. Seidl, R.; Schelhaas, M.J.; Rammer, W.; Verkerk, P.J. Increasing forest disturbances in Europe and their impact on carbon storage. *Nat. Clim. Change* **2014**, *4*, 806–810. [CrossRef]
3. Sangüesa-Barreda, G.; Camarero, J.J.; Oliva, J.; Montes, F.; Gazol, A. Past logging, drought and pathogens interact and contribute to forest dieback. *Agric. For. Meteorol.* **2015**, *208*, 85–94. [CrossRef]
4. Netherer, S.; Schopf, A. Potential effects of climate change on insect herbivores in European forests—General aspects and the pine processionary moth as specific example. *For. Ecol. Manag.* **2010**, *259*, 831–838. [CrossRef]
5. Hamann, E.; Blevins, C.; Franks, S.J.; Jameel, M.I.; Anderson, J.T. Climate change alters plant–herbivore interactions. *New Phytol.* **2021**, *229*, 1894–1910. [CrossRef]
6. Batllori, E.; Lloret, F.; Aakala, T.; Anderegg, W.R.L.; Aynekulu, E.; Bendixsen, D.P.; Bentouati, A.; Bigler, C.; Burk, C.J.; Camarero, J.J.; et al. Forest and woodland replacement patterns following drought-related mortality. *Proc. Natl. Acad. Sci. USA* **2020**, *117*, 29720–29729. [CrossRef]
7. Bowman, D.M.J.S.; Williamson, G.J.; Abatzoglou, J.T.; Kolden, C.A.; Cochrane, M.A.; Smith, A.M.S. Human exposure and sensitivity to globally extreme wildfire events. *Nat. Ecol. Evol.* **2017**, *1*, 58. [CrossRef]

8. Tramblay, Y.; Koutroulis, A.; Samaniego, L.; Vicente-Serrano, S.M.; Volaire, F.; Boone, A.; Le Page, M.; Llasat, M.C.; Albergel, C.; Burak, S.; et al. Challenges for drought assessment in the Mediterranean region under future climate scenarios. *Earth-Sci. Rev.* **2020**, *210*, 103348. [CrossRef]
9. Montes, F.; Sánchez, M.; Del Río, M.; Cañellas, I. Using historic management records to characterize the effects of management on the structural diversity of forests. *For. Ecol. Manag.* **2005**, *207*, 279–293. [CrossRef]
10. Gea-Izquierdo, G.; Sánchez-González, M. Forest disturbances and climate constrain carbon allocation dynamics in trees. *Glob. Change Biol.* **2022**, *28*, 4342–4358. [CrossRef]
11. Dye, A.W.; Houtman, R.M.; Gao, P.; Anderegg, W.R.L.; Fettig, C.J.; Hicke, J.A.; Kim, J.B.; Still, C.J.; Young, K.; Riley, K.L. Carbon, climate, and natural disturbance: A review of mechanisms, challenges, and tools for understanding forest carbon stability in an uncertain future. *Carbon Bal. Manag.* **2024**, *19*, 35. [CrossRef]
12. Muys, B.; Angelstam, P.; Bauhus, J.; Bouriaud, L.; Jactel, H.; Kraigher, H.; Müller, J.; Pettorelli, N.; Pötzelsberger, E.; Primmer, E.; et al. *Forest Biodiversity in Europe. From Science to Policy 13*; European Forest Institute: Joensuu, Finland, 2022. [CrossRef]
13. Thom, D.; Seidl, R. Natural disturbance impacts on ecosystem services and biodiversity in temperate and boreal forests. *Bilogical Rev.* **2015**, *91*, 760–781. [CrossRef]
14. Korhonen, K.T.; Huuskonen, S.; Kolström, T.; Kurttila, M.; Punttila, P.; Siitonen, J. Closer-to-nature forest management approaches in Finland. In *Natural Resources and Bioeconomy Studies*; Natural Resources Institute Finland: Helsinki, Finland, 2021; Volume 83/2021, 25p. Available online: https://urn.fi/URN:ISBN:978-952-380-314-5 (accessed on 5 February 2026).
15. Nikinmaa, L.; de Koning, J.H.C.; Derks, J.; Grabska-Szwagrzyk, E.; Konczal, A.A.; Lindner, M.; Socha, J.; Muys, B. The priorities in managing forest disturbances to enhance forest resilience: A comparison of a literature analysis and perceptions of forest professionals. *For. Policy Econ.* **2024**, *158*, 103119. [CrossRef]
16. Lister, A.J.; Andersen, H.; Frescino, T.; Gatziolis, D.; Healey, S.; Heath, L.S.; Liknes, G.C.; McRoberts, R.; Moisen, G.G.; Nelson, M.; et al. Use of Remote Sensing Data to Improve the Efficiency of National Forest Inventories: A Case Study from the United States National Forest Inventory. *Forests* **2020**, *11*, 1364. [CrossRef]
17. Hlásny, T.; Perunová, M.; Modlinger, R.; Blake, M.; Brazaitis, G.; Csóka, G.; De Groot, M.; Duduman, M.L.; Faccoli, M.; Georgieva, M.; et al. Perspectives: State of national forest damage survey programmes in Europe and ways toward improved harmonization and data sharing. *For. Ecol. Manag.* **2025**, *597*, 123111. [CrossRef]
18. Fassnacht, F.E.; White, J.C.; Wulder, M.A.; Næsset, E. Remote sensing in forestry: Current challenges, considerations and directions. *Forestry* **2023**, *97*, 11–37. [CrossRef]
19. Gómez, C.; Alejandro, P.; Hermosilla, T.; Montes, F.; Pascual, C.; Ruiz, L.A.; Álvarez-Taboada, F.; Tanase, M.A.; Valbuena, R. Remote sensing for the Spanish forests in the 21st century: A review of advances, needs, and opportunities. *For. Syst.* **2019**, *28*, eR001. [CrossRef]
20. Kennedy, R.E.; Yang, Z.; Cohen, W.B. Detecting trends in forest disturbance and recovery using yearly Landsat time series: 1. LandTrendr—Temporal segmentation algorithms. *Remote Sens. Environ.* **2010**, *114*, 2897–2910. [CrossRef]
21. Hermosilla, T.; Wulder, M.A.; White, J.C.; Coops, N.C.; Hobart, G.W. An integrated Landsat time series protocol for change detection and generation of annual gap-free surface reflectance composites. *Remote Sens. Environ.* **2015**, *158*, 220–234. [CrossRef]
22. Zhu, Z.; Woodcock, C. Continuous change detection and classification of land cover using all available Landsat data. *Remote Sens. Environ.* **2014**, *144*, 152–171. [CrossRef]
23. Pacheco-Pascagaza, A.M.; Gou, Y.; Louis, V.; Roberts, J.F.; Rodríguez-Veiga, P.; Bispo, P.C.; Espírito-Santo, F.D.B.; Robb, C.; Upton, C.; Galindo, G.; et al. Near real-time change detection system using Sentinel-2 and machine learning: A test for Mexican and Colombian forests. *Remote Sens.* **2022**, *14*, 707. [CrossRef]
24. Jiang, J.; Xing, Y.; Wei, W.; Yan, E.; Xiang, J.; Mo, D. DSNUNet: An improved forest change detection network by combining Sentinel-1 and Sentinel-2 images. *Remote Sens.* **2022**, *14*, 5046. [CrossRef]
25. Migas-Mazur, R.; Kycko, M.; Zwijacz-Kozica, T.; Zagajewski, B. Assessment of Sentinel-2 images, support vector machines and change detection algorithms for bark beetle outbreaks mapping in the Tatra Mountains. *Remote Sens.* **2021**, *13*, 3314. [CrossRef]
26. Bozzini, A.; Francini, S.; Chirici, G.; Battisti, A.; Faccoli, M. Spruce bark beetle outbreak prediction through automatic classification of Sentinel-2 imagery. *Forests* **2023**, *14*, 1116. [CrossRef]
27. D'Amico, G.; Francini, S.; Parisi, F.; Vangi, E.; De Santis, E.; Travaglini, D.; Chirici, G. Multitemporal optical remote sensing to support forest health condition assessment of Mediterranean pine forests in Italy. In *Global Challenges for a Sustainable Society*; Benítez-Andrades, J.A., García-Llamas, P., Taboada, Á., Estévez-Mauriz, L., Baelo, R., Eds.; EURECA-PRO 2022; Springer Proceedings in Earth and Environmental Sciences; Springer: Cham, Switzerland, 2023; pp. 113–123.
28. Falanga, V.; Francini, S.; Parisi, F.; Cavalli, A.; De Fioravante, P.; Cucca, B.; D'Amico, G.; Chirici, G.; Lasserre, B.; Ottaviano, M.; et al. Near-Real-Time Detection of Insect Outbreaks in Urban Trees Using a PlanetScope Time Series. *Forests* **2024**, *15*, 2261. [CrossRef]
29. Decuyper, M.; Chávez, R.O.; Lohbeck, M.; Lastra, J.A.; Tsendbazar, N.; Hackländer, J.; Herold, M.; Vågen, T.G. Continuous monitoring of forest change dynamics with satellite time series. *Remote Sens. Environ.* **2022**, *269*, 112829. [CrossRef]

30. Ahangarha, M.; Shah-Hosseini, R.; Saadatseresht, M. Deep learning-based change detection method for environmental change monitoring using Sentinel-2 datasets. *Environ. Sci. Proc.* **2021**, *5*, 15. [CrossRef]
31. Miguel, S.; Ruiz-Benito, P.; Rebollo, P.; Viana-Soto, A.; Mihai, M.C.; García-Martín, A.; Tanase, M. Forest disturbance regimes and trends in continental Spain (1985–2023) using dense Landsat time series. *Environ. Res.* **2024**, *262*, 119802. [CrossRef]
32. Chirici, G.; Giannetti, F.; Mazza, E.; Francini, S.; Travaglini, D.; Pegna, R.; White, J.C. Monitoring clearcutting and subsequent rapid recovery in Mediterranean coppice forests with Landsat time series. *Ann. For. Sci.* **2020**, *77*, 40. [CrossRef]
33. Valladares, F.; Benavides, R.; Rabasa, S.; Díaz, M.; Pausas, J.; Paula, S.; Simonson, W. Global change and Mediterranean forest: Current impacts and potential responses. In *Forests and Global Change*; Coomes, D.A., Burslem, D.F.R.P., Simonson, W.D., Eds.; Cambridge University Press: Cambridge, UK, 2013; pp. 47–75. [CrossRef]
34. Francini, S.; McRoberts, R.E.; Giannetti, F.; Marchetti, M.; Scarascia Mugnozza, G.; Chirici, G. The Three Indices Three Dimensions (3I3D) algorithm: A new method for forest disturbance mapping and area estimation based on optical remotely sensed imagery. *Int. J. Remote Sens.* **2021**, *42*, 4693–4711. [CrossRef]
35. Francini, S.; Chirici, G. A Sentinel-2 derived dataset of forest disturbances occurred in Italy between 2017 and 2020. *Data Brief* **2022**, *42*, 108297. [CrossRef]
36. Vangi, E.; D'Amico, G.; Francini, S.; Borghi, C.; Giannetti, F.; Corona, P.; Marchetti, M.; Travaglini, D.; Pellis, G.; Vitullo, M.; et al. Large-scale high-resolution yearly modelling of forest growing stock volume and above-ground carbon pool. *Environ. Model. Softw.* **2023**, *159*, 105580. [CrossRef]
37. Cavalli, A.; Francini, S.; McRoberts, R.E.; Falanga, V.; Congedo, L.; De Fioravante, P.; Maesano, M.; Munafò, M.; Chirici, G.; Scarascia-Mugnozza, G. Estimating afforestation area using Landsat time series and photointerpreted datasets. *Remote Sens.* **2023**, *15*, 923. [CrossRef]
38. Francini, S.; Cavalli, A.; D'Amico, G.; McRoberts, R.E.; Maesano, M.; Munafò, M.; Scarascia-Mugnozza, G.; Chirici, G. Reusing remote sensing-based validation data: Comparing direct and indirect approaches for afforestation monitoring. *Remote Sens.* **2023**, *15*, 1638. [CrossRef]
39. Francini, S.; D'Amico, G.; Vangi, E.; Borghi, C.; Chirici, G. Integrating GEDI and Landsat: Spaceborne lidar and four decades of optical imagery for the analysis of forest disturbances and biomass changes in Italy. *Sensors* **2022**, *22*, 2015. [CrossRef] [PubMed]
40. Hansen, M.C.; Potapov, P.V.; Moore, R.; Hancher, R.; Turubanova, S.A.; Tyukavina, A.; Thau, D.; Stehman, S.V.; Goetz, S.J.; Loveland, T.R.; et al. High-resolution global maps of 21st-century forest cover change. *Science* **2013**, *342*, 850–853. [CrossRef] [PubMed]
41. Giannetti, F.; Pegna, R.; Francini, S.; McRoberts, R.E.; Travaglini, D.; Marchetti, M.; Scarascia-Mugnozza, G.; Chirici, G. A new method for automated clearcut disturbance detection in Mediterranean coppice forests using Landsat time series. *Remote Sens.* **2020**, *12*, 3720. [CrossRef]
42. Cardille, J.A.; Perez, E.; Crowley, M.A.; Wulder, M.A.; White, J.C.; Hermosilla, T. Multi-sensor change detection for within-year capture and labelling of forest disturbance. *Remote Sens. Environ.* **2022**, *268*, 112741. [CrossRef]
43. Hermosilla, T.; Wulder, M.A.; White, J.C.; Coops, N.C.; Hobart, G.W. Regional detection, characterization, and attribution of annual forest change from 1984 to 2012 using Landsat-derived time-series metrics. *Remote Sens. Environ.* **2015**, *170*, 121–132. [CrossRef]
44. Morin-Bernard, A.; Achim, A.; Coops, N.C. Attributing a causal agent and assessing the severity of non-stand replacing disturbances in a northern hardwood forest using Landsat-derived vegetation indices. *Can. J. Remote Sens.* **2023**, *49*, 2196356. [CrossRef]
45. Oeser, J.; Pflugmacher, D.; Senf, C.; Heurich, M.; Hostert, P. Using intra-annual Landsat time series for attributing forest disturbance agents in Central Europe. *Forests* **2017**, *8*, 251. [CrossRef]
46. Nguyen, T.H.; Jones, S.D.; Soto-Berelov, M.; Haywood, A.; Hislop, S. A spatial and temporal analysis of forest dynamics using Landsat time-series. *Remote Sens. Environ.* **2018**, *217*, 461–475. [CrossRef]
47. Pasquarella, V.J.; Arévalo, P.; Bratley, K.H.; Bullock, E.L.; Gorelick, N.; Yang, Z.; Kennedy, R.E. Demystifying LandTrendr and CCDC temporal segmentation. *Int. J. Appl. Earth Obs. Geoinf.* **2022**, *110*, 102806. [CrossRef]
48. Bonannella, C.; Chirici, G.; Travaglini, D.; Pecchi, M.; Vangi, E.; D'Amico, G.; Giannetti, F. Characterization of wildfires and harvesting forest disturbances and recovery using Landsat time series: A case study in Mediterranean forests in Central Italy. *Fire* **2022**, *5*, 68. [CrossRef]
49. Chirici, G.; Giuliarelli, D.; Biscontini, D.; Tonti, D.; Mattioli, W.; Marchetti, M.; Corona, P. Large-scale monitoring of coppice forest clearcuts by multitemporal very high resolution satellite imagery. A case study from central Italy. *Remote Sens. Environ.* **2011**, *115*, 1025–1033. [CrossRef]
50. Morresi, D.; Maeng, H.; Marzano, R.; Lingua, E.; Motta, R.; Garbarino, M. High-dimensional detection of landscape dynamics: A Landsat time series-based algorithm for forest disturbance mapping and beyond. *GISci. Remote Sens.* **2024**, *61*, 2365001. [CrossRef]
51. IEPNB. Informe Anual 2024 Sobre el Estado del Patrimonio Natural y de la Biodiversidad en España. 2026. Available online: https://libreria.miteco.gob.es/media/miteco/files/book-attachment-42.pdf (accessed on 5 February 2026).

52. MITECO. Spanish Forest Map. Foto fija 2018. Available online: https://www.miteco.gob.es/es/biodiversidad/temas/inventarios-nacionales/mapa-forestal-espana/foto_fija_mfe.html (accessed on 1 February 2024).
53. Gorelick, N.; Hancher, M.; Dixon, M.; Ilyushchenko, S.; Thau, D.; Moore, R. Google Earth Engine: Planetary-scale geospatial analysis for everyone. *Remote Sens Environ.* **2017**, *202*, 18–27. [CrossRef]
54. Francini, S.; Hermosilla, T.; Coops, N.C.; Wulder, M.A.; White, J.C.; Chirici, G. An assessment approach for pixel-based image composites. *ISPRS J. Photogramm. Remote Sens.* **2023**, *202*, 1–12. [CrossRef]
55. Goward, S.N.; Williams, D.L.; Arvidson, T.; Rocchio, L.E.P.; Irons, J.R.; Russell, C.A.; Johnston, S.S. *Landsat's Enduring Legacy: Pioneering Global Land Observations from Space*; American Society for Photogrammetry and Remote Sensing: Bethesda, MD, USA, 2017; 586p.
56. Parisi, F.; Elia, V.; Saverio, F.; D'Amico, G.; Chirici, G.; Marchetti, M.; Lombardi, F.; Travaglini, D.; Ravera, S.; De Santis, E.; et al. Sentinel-2 time series analysis for monitoring multi-taxon biodiversity in mountain beech forests. *Frontiers* **2023**, *6*, 1020477. [CrossRef]
57. Flood, N. Seasonal composite Landsat TM/ETM+ images using the medoid (a multi-dimensional median). *Remote Sens.* **2013**, *5*, 6481–6500. [CrossRef]
58. Schultz, M.; Li, H.; Wu, Z.; Wiell, D.; Auer, M.; Alexander, Z. OSMlanduse a dataset of European Union land use at 10 m resolution derived from OpenStreetMap and Sentinel-2. *Sci. Data* **2025**, *12*, 750. [CrossRef] [PubMed]
59. 3I3D-GEE. Available online: https://github.com/saveriofrancini/AreaEstimator3I3DGEE (accessed on 3 June 2024).
60. Jonckheere, I.; Hamilton, R.; Michel, J.M.; Donegan, E. (Eds.) *Good Practices in Sample-Based Area Estimation*; White paper; FAO: Rome, Italy, 2024. [CrossRef]
61. PNOA. Available online: https://pnoa.ign.es/ (accessed on 3 June 2024).
62. Google Earth™. Available online: https://earth.google.com (accessed on 3 June 2024).
63. Coops, N.C.; Shang, C.; Wulder, M.A.; White, J.C.; Hermosilla, T. Change in forest condition: Characterizing non-stand replacing disturbances using time series satellite imagery. *For. Ecol. Manag.* **2020**, *474*, 118370. [CrossRef]
64. Boser, B.E.; Guyon, I.M.; Vapnik, V.N. A training algorithm for optimal margin classifiers. In Proceedings of the COLT92: 5th Annual Workshop on Computational Learning Theory, Pittsburgh, PA, USA, 27–29 July 1992; pp. 144–152. [CrossRef]
65. Mountrakis, G.; Im, J.; Ogole, C. Support vector machines in remote sensing: A review. *ISPRS J. Photogramm. Remote Sens.* **2011**, *66*, 247–259. [CrossRef]
66. Breiman, L. Random Forests. *Mach. Learn.* **2001**, *45*, 5–32. [CrossRef]
67. Mas, J.F.; Flores, J.J. The application of artificial neural networks to the analysis of remotely sensed data. *Int. J. Remote Sens.* **2008**, *29*, 617–663. [CrossRef]
68. D'Amico, G.; Francini, S.; Giannetti, F.; Vangi, E.; Travaglini, D.; Chianucci, F.; Chirici, G. A deep learning approach for automatic mapping of poplar plantations using Sentinel-2 imagery. *GISci. Remote Sens.* **2021**, *58*, 1352–1368. [CrossRef]
69. Francini, S.; Cocozza, C.; Hölttä, T.; Lintunen, A.; Paljakka, T.; Chirici, G.; Traversi, M.L.; Giovannelli, A. A temporal segmentation approach for dendrometers signal-to-noise discrimination. *Comput. Electron. Agric.* **2023**, *210*, 107925. [CrossRef]
70. Hawrylo, P.; Francini, S.; Chirici, G.; Giannetti, F.; Parkitna, K.; Krok, G.; Mitelsztedt, K.; Lisańczuk, M.; Stereńczak, K.; Ciesielski, M.; et al. The use of remotely sensed data and Polish NFI plots for prediction of growing stock volume using different predictive methods. *Remote Sens.* **2020**, *12*, 3331. [CrossRef]
71. Valavi, R.; Guillera-Arroita, G.; Lahoz-Monfort, J.; Elith, J. Predictive performance of presence-only species distribution models: A benchmark study with reproducible code. *Ecol. Monogr.* **2022**, *92*, e1486:1–27. [CrossRef]
72. Hughes-Oliver, J. Population and empirical PR curves for assessment of ranking algorithms. *arXiv* **2018**, arXiv:1810.08635. [CrossRef]
73. Matthews, B. Comparison of the predicted and observed secondary structure of T4 phage lysozyme. *Biochim. Biophys. Acta Protein Struct.* **1975**, *2*, 442–451. [CrossRef] [PubMed]
74. Olofsson, P.; Foody, G.M.; Herold, M.; Stehman, S.V.; Woodcock, C.E.; Wulder, M.A. Good practices for estimating area and assessing accuracy of land change. *Remote Sens. Environ.* **2014**, *148*, 42–457. [CrossRef]
75. Mantero, G.; Morresi, D.; Marzano, R.; Motta, R.; Mladenoff, D.; Garbarino, M. The influence of land abandonment on forest disturbance regimes: A global review. *Landsc. Ecol.* **2020**, *35*, 2723–2744. [CrossRef]
76. Chirici, G.; Chiesi, M.; Fibbi, L.; Giannetti, F.; Corona, P.; Maselli, F. High spatial resolution modelling of net forest carbon fluxes based on ground and remote sensing data. *Agric. For. Meteorol.* **2022**, *316*, 108866. [CrossRef]
77. Pitkänen, T.P.; Sirro, L.; Häme, L.; Häme, T.; Törmä, M.; Kangas, A. Errors related to the automatized satellite-based change detection of boreal forests in Finland. *Int. J. Appl. Earth Obs. Geoinf.* **2020**, *86*, 102011. Available online: http://hdl.handle.net/10138/336902 (accessed on 1 February 2024). [CrossRef]
78. Li, Y.; Xu, X.; Wu, Z.; Fan, H.; Tong, X.; Liu, J. A forest type-specific threshold method for improving forest disturbance and agent attribution mapping. *GISci. Remote Sens.* **2022**, *59*, 1624–1642. [CrossRef]

79. Jarron, L.R.; Hermosilla, T.; Coops, N.C.; Wulder, M.A.; White, J.C.; Hobart, G.W.; Leckie, D.G. Differentiation of alternate harvesting practices using annual time series of Landsat data. *Forests* **2017**, *8*, 15. [CrossRef]
80. Altalhan, M.; Algarni, A.; Turki-Hadj Alouane, M. Imbalanced Data Problem in Machine Learning: A Review. *IEEE Access* **2025**, *13*, 13686–13699. [CrossRef]
81. Bradter, U.; Altringham, J.D.; Kunin, W.E.; Thom, T.J.; O'Connell, J.; Benton, T.G. Variable ranking and selection with random forest for unbalanced data. *Environ. Data Sci.* **2022**, *1*, e30. [CrossRef]
82. Griffiths, P.; Kuemmerle, T.; Baumann, M.; Radeloff, V.C.; Abrudan, I.V.; Lieskovsky, J.; Munteanu, C.; Ostapowicz, K.; Hostert, P. Forest disturbances, forest recovery, and changes in forest types across the Carpathian ecoregion from 1985 to 2010 based on Landsat image composites. *Remote Sens. Environ.* **2014**, *151*, 72–88. [CrossRef]
83. Collins, L.; Griffioen, P.; Newell, G.; Mellor, A. The utility of random forests for wildfire severity mapping. *Remote Sens. Environ.* **2018**, *216*, 374–384. [CrossRef]
84. Arévalo, P.; Olofsson, P.; Woodcock, C.E. Continuous monitoring of land change activities and post-disturbance dynamics from Landsat time series: A test methodology for REDD+ reporting. *Remote Sens. Environ.* **2020**, *238*, 111051. [CrossRef]
85. Bullock, E.L.; Woodcock, C.E.; Holden, C.E. Improved change monitoring using an ensemble of time series algorithms. *Remote Sens. Environ.* **2020**, *238*, 111165. [CrossRef]
86. Carter, G.; Wagner, F.H.; Dalagnol, R.; Roberts, S.; Ritz, A.L.; Saatchi, S. Detection of forest disturbance across California using deep-learning on PlanetScope imagery. *Front. Remote Sens.* **2024**, *5*, 1409400. [CrossRef]
87. Chen, X.; Zhao, W.; Chen, J.; Qu, Y.; Wu, D.; Chen, X. Mapping Large-Scale Forest Disturbance Types with Multi-Temporal CNN Framework. *Remote Sens.* **2021**, *13*, 5177. [CrossRef]
88. Masolele, R.N.; De Sy, V.; Herold, M.; Marcos, D.; Verbesselt, J.; Gieseke, F.; Mullissa, A.G.; Martius, C. Spatial and temporal deep learning methods for deriving land-use following deforestation: A pan-tropical case study using Landsat time series. *Remote Sens. Environ.* **2021**, *264*, 112600. [CrossRef]
89. Solórzano, J.V.; Gao, Y. Forest Disturbance Detection with Seasonal and Trend Model Components and Machine Learning Algorithms. *Remote Sens.* **2022**, *14*, 803. [CrossRef]
90. Paulino, E.R.; Schlerf, M.; Röder, A.; Stoffels, J.; Udelhoven, T. Forest disturbance characterization in the era of earth observation big data: A mapping review. *Int. J. Appl. Earth Obs. Geoinf.* **2024**, *128*, 103755. [CrossRef]
91. Southworth, J.; Smith, A.C.; Safaei, M.; Rahaman, M.; Alruzuq, A.; Tefera, B.B.; Muir, C.S.; Herrero, H.V. Machine learning versus deep learning in land system science: A decision-making framework for effective land classification. *Front. Remote Sens.* **2024**, *5*, 1374862. [CrossRef]
92. Cohen, W.B.; Yang, Z.; Healey, S.P.; Kennedy, R.E.; Gorelick, N. A LandTrendr multispectral ensemble for forest disturbance detection. *Remote Sens. Environ.* **2018**, *205*, 131–140. [CrossRef]
93. Esteban, J.; Fernández-Landa, A.; Tomé, J.L.; Gómez, C.; Marchamalo, M. Identification of silvicultural practices in Mediterranean forests integrating Landsat time series and a single coverage of ALS data. *Remote Sens.* **2021**, *13*, 3611. [CrossRef]
94. Pickens, A.H.; Hansen, M.C.; Song, Z.; Poulson, A.; Komarova, A.; Baggett, A.; Kerr, T.; Mikus, A.; Ortiz-Domínguez, C.; Tyukavina, A.; et al. Rapid monitoring of global land change. *Nat. Commun.* **2025**, *16*, 8948. [CrossRef] [PubMed]
95. Web-Based Global Forest Change 2000–2024. Available online: https://glad.earthengine.app/view/global-forest-change (accessed on 5 February 2026).
96. Land Monitoring Service of Copernicus—Burnt Area 2018-Present (Raster 300 m), Global, Monthly—Version 4. Available online: https://doi.org/10.2909/8fa58061-28ab-49bb-9b77-c26b50733e34 (accessed on 5 February 2026).
97. GWIS Annual Statistics for Spain. Available online: https://gwis.jrc.ec.europa.eu/apps/gwis.statistics/estimates (accessed on 5 February 2026).
98. MITECO. Los Incendios Forestales en España. 1 de Enero 2018–31 de Diciembre 2018. Avance Informativo. 2019. Available online: https://www.miteco.gob.es/content/dam/miteco/es/biodiversidad/temas/incendios-forestales/iiff_2018_tcm30-521614.pdf (accessed on 3 June 2024).
99. Karlson, M.; Reese, H.; Ostwald, M. Tree crown mapping in managed woodlands (parklands) of semi-arid West Africa using Worldview-2 imagery and geographic object-based image analysis. *Sensors* **2014**, *14*, 22643–22669. [CrossRef] [PubMed]
100. Ji, Z.; Xu, J.; Yan, L.; Ma, J.; Chen, B.; Zhang, Y.; Zhang, L.; Wang, P. Satellite remote sensing images of crown segmentation and forest inventory based on BlendMask. *Forests* **2024**, *15*, 1320. [CrossRef]
101. Sun, C.; Huang, C.; Zhang, H.; Chen, B.; An, F.; Wang, L.; Yun, T. Individual tree crown segmentation and crown width extraction from a heightmap derived from aerial laser scanning data using a deep learning framework. *Front. Plant Sci.* **2022**, *13*, 914974. [CrossRef]